Probabilistic density maps to study global endomembrane organization

Kristine Schauer[1], Tarn Duong[1,2], Kevin Bleakley[3], Sabine Bardin[1], Michel Bornens[1] & Bruno Goud[1]

We developed a computational imaging approach that describes the three-dimensional spatial organization of endomembranes from micromanipulation-normalized mammalian cells with probabilistic density maps. Applied to several well-known marker proteins, this approach revealed the average steady-state organization of early endosomes, multivesicular bodies or lysosomes, endoplasmic reticulum exit sites, the Golgi apparatus and Golgi-derived transport carriers in crossbow-shaped cells. The steady-state organization of each tested endomembranous population was well-defined, unique and in some cases depended on the cellular adhesion geometry. Density maps of all endomembrane populations became stable when pooling several tens of cells only and were reproducible in independent experiments, allowing construction of a standardized cell model. We detected subtle changes in steady-state organization induced by disruption of the cellular cytoskeleton, with statistical significance observed for just 20 cells. Thus, combining micropatterning with construction of endomembrane density maps allows the systematic study of intracellular trafficking determinants.

The intracellular membrane system of eukaryotic cells comprises a variety of endomembranes including nuclear envelope, endoplasmic reticulum, Golgi apparatus, endosomes and tubular-vesicular transport carriers, connected by multiple routes. Many studies have highlighted the complexity of transport pathways that permit constant exchange between intracellular compartments. To tackle this complexity, it is crucial to develop quantitative methods to better understand topological relationships between membrane trafficking compartments.

Although the organization of the intracellular membrane system is not known, it is intimately linked to cell cytoskeleton architecture[1]. Membranous transport carriers shuttling between compartments move along microtubules or are tethered and displaced on actin networks via molecular motors[2–4]. One difficulty in studying endomembrane organization is that the connection between transport and cytoskeleton goes both ways: transport events also strongly influence cell cytoskeleton architecture. For instance, during cell migration, precise delivery of proteins and lipids to the leading edge helps to induce reorganization of cortical actin and reorientation of the microtubule network along the migration axis[5,6]. Also, endosomes and the Golgi apparatus have the capacity to respectively nucleate actin and microtubules[7–10]. The consequence of this interdependence is that cell morphology varies over time; cells are moving and constantly disassemble and reassemble their cytoskeleton. Furthermore, cells grown in culture often display strong morphological cell-to-cell variation in a given population[11,12]. Population size, local cell density and position in a cellular islet have all been shown to determine cellular morphology and responsiveness[13]. The resulting heterogeneity limits the systematic study of the global organization of trafficking endomembranes. Unlike the compact Golgi apparatus in mammalian cells and the endocytic recycling compartment, endosomes and various transport carriers are spatially dispersed and difficult to quantify. The large number of structures belonging to endomembranous populations (such as early endosomes) makes studying their organization challenging.

To avoid the limitations of classical approaches that use unconstrained, dynamic cell shapes, we used microfabricated patterns, which enforce cells to take a certain shape and prevent their migration[14]. Micropatterns allow for control of organelle organization[15,16], and we ascertained a normal cell cycle and thus functional integrity. These patterned cells allowed us to construct quantitative maps of the spatial organization of intracellular membranous compartments and to detect subtle changes in endomembrane organization induced by cytoskeleton disruption.

RESULTS

Construction of probabilistic endomembrane maps

We grew telomerase-immortalized human RPE-1 cells on crossbow-shaped patterns, which biased the internal cellular organization along an anterior-posterior polar axis[16]. Vinculin-containing focal adhesion sites form along the adhesive edges of the ‘bow’, and stress fibers are enriched at nonadhesive areas of the ‘string’[16] (**Supplementary Fig. 1a**). We grew cells on patterns for 3 h before fixing them and immunodetecting endomembranes by

---

[1] Unité Mixte de Recherche 144, Centre National de la Recherche Scientifique, Institut Curie, Laboratory Molecular Mechanisms of Intracellular Transport, Paris, France. [2] Institut Pasteur, Groupe Imagerie et Modélisation, Unité de Recherche Associée 2582, Centre National de la Recherche Scientifique, Paris, France. [3] Mines ParisTech, Centre for Computational Biology, Institut Curie, Institut National de la Santé Et de la Recherche Médicale U900, Paris, France. Correspondence should be addressed to K.S. (kristine.schauer@curie.fr) or B.G. (bruno.goud@curie.fr).

RECEIVED 8 FEBRUARY; ACCEPTED 26 MARCH; PUBLISHED ONLINE 30 MAY 2010; DOI:10.1038/NMETH.1462

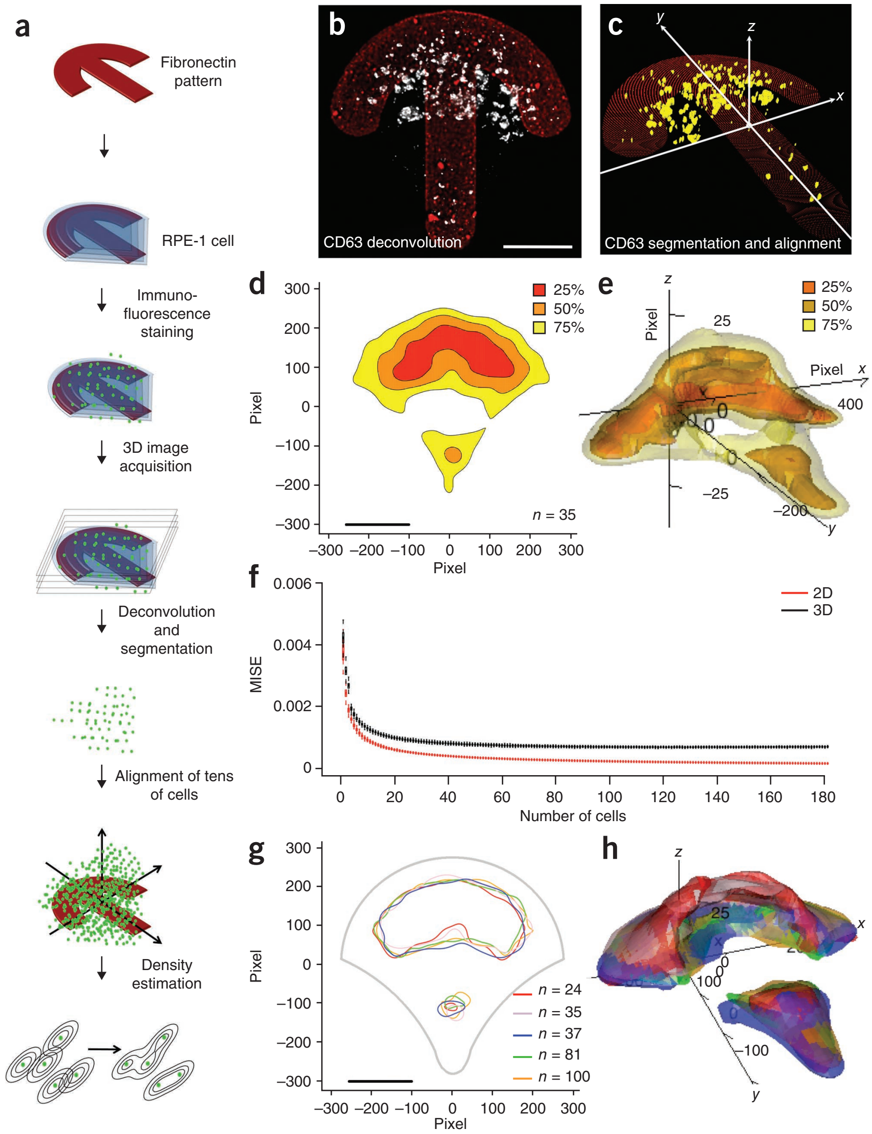

Figure 1 | Analysis of CD63-positive endomembranes from 35 cells on crossbow-shaped patterns. (**a**) Outline of experimental procedure. (**b**) Maximum intensity projection of the deconvolved fluorescence of CD63-positive endomembranes (white) and the fluorescently marked crossbow pattern (red). (**c**) Schematic representation of the segmentation and alignment procedure using the fluorescently marked crossbow pattern. (**d**) The 2D density estimation map with the indicated percentile probability contours representing the smallest regions in which the corresponding percentage of CD63-positive endomembranes were found. (**e**) The 3D density estimation map. For ease of visualization, the height (*z* axis) has been stretched fivefold. (**f**) Estimated MISE for 2D and 3D density estimation as a function of the number of CD63-positive cells analyzed. (**g**) Overlap of the 50% contour of the 2D estimation for five independent experiments. Each color represents an independent experiment using *n* cells. The outer gray outline represents spread of crossbow-shaped cells. (**h**) Overlap of the 50% contour of the 3D estimation for five independent experiments; color-code for independent experiments as in **g**. Scale bars, 10 μm.

marker proteins and fluorophore-coupled antibodies; alternatively, we constructed stable cell lines expressing EGFP-tagged marker proteins that we directly analyzed after fixing the cells. We acquired three-dimensional (3D) image stacks of several tens of cells (**Supplementary Table 1**) and deconvolved them (**Fig. 1a**). We extracted positional information of fluorescently labeled endomembranes from each single cell by segmentation analysis using multi-dimensional image analysis[17] and aligned coordinates using characteristic landmarks of micropatterns. To examine the average steady-state spatial organization of each endomembrane population, we calculated its probability density throughout the cell using a kernel density estimator available for the R software. Briefly, Gaussian functions (kernels) with mean zero and an optimized variance were centered at each of the data points and summed, revealing the underlying density throughout the cell. Typically, we used several thousand coordinates to calculate the density function (**Supplementary Table 1**). To visualize the result, we calculated equally spaced probability contours[18,19]. Contours represent the smallest area in which a given percentage of endomembranes are found: for example, the 50% probability contour defines the smallest area in which 50% of endomembranes are located. As several equally dense yet separated regions can appear in the cell, a given probability contour can be located in several different places in the cell.

First, we analyzed the spatial distribution of CD63 using 35 crossbow-shaped cells (**Fig. 1b**,**c**). CD63 is a transmembrane protein and a well-established marker protein of multivesicular bodies or lysosomes[20]. We first ignored the height coordinate and considered the density in two dimensions, which revealed well-defined organization (**Fig. 1d**); CD63 predominantly localized to a region close to the bow-shaped attachment zone of the crossbow pattern (**Supplementary Fig. 1a**). However, as cells grown on flat surfaces are thicker at the center than at the periphery, two-dimensional (2D) density estimation tends to exaggerate the density at the cell center. To remove this bias, we calculated probability contours in three dimensions (**Fig. 1e**). Consistent with the 2D map, immunodetected CD63-positive endosomes occupied a volume close to the adhesion region of the crossbow pattern.

To estimate the reliability of density maps, we computed the statistical error of the CD63 density estimation as a function of the number of cells analyzed. We defined the statistical error as the estimated mean integrated squared error (MISE) and calculated it in two and three dimensions for up to 181 cells containing on average 300 endomembranes per cell (**Fig. 1f**). For less than 20 cells, the box plots of estimated MISEs showed a large variability in both two and three dimensions, with drastic improvement in estimated MISE when adding data for each subsequent cell. The estimated MISE only marginally diminished for 20–50 cells and virtually did not change thereafter. This demonstrated that using density estimation with micropatterned cells is robust with only several tens of cells.

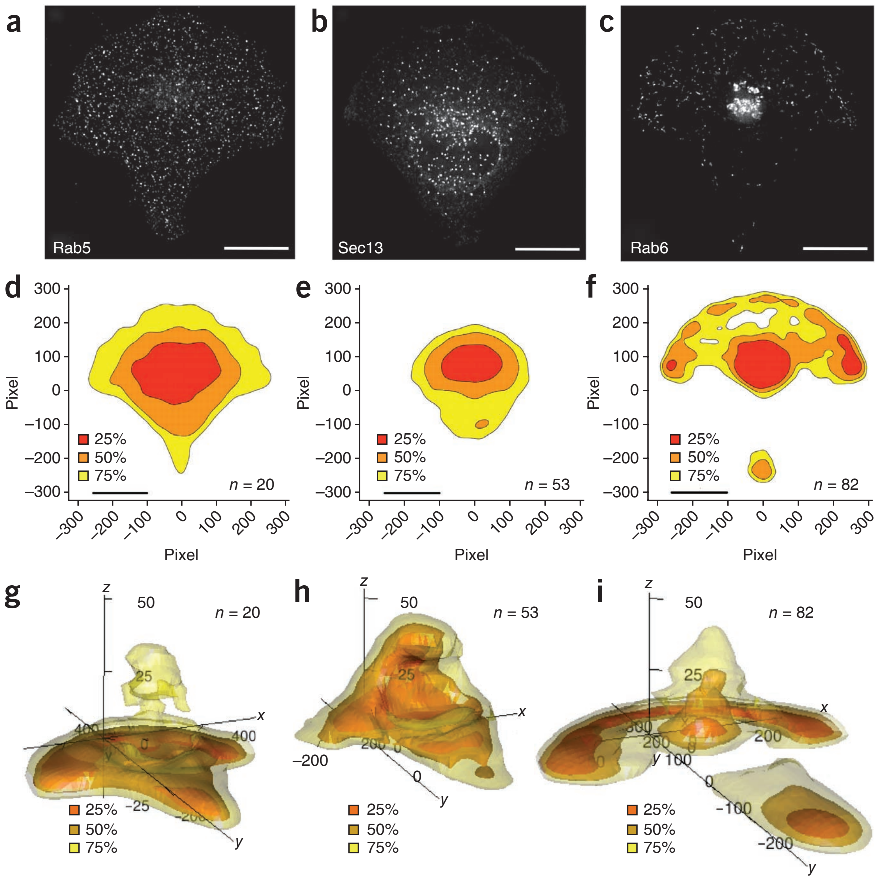

Figure 2 | Analysis of Rab5-, Sec13- and Rab6-positive endomembranes on crossbow-shaped patterns. (**a**–**c**) Maximum intensity projection of the deconvolved fluorescence of Rab5-positive (**a**), Sec13-positive (**b**) and Rab6-positive (**c**) endomembranes. (**d**–**f**) The 2D density estimations of Rab5-positive endomembranes from 20 cells (**d**), Sec13-positive endomembranes from 53 cells (**e**) and Rab6-positive endomembranes from 82 cells (**f**). (**g**–**i**) The 3D density estimations of Rab5-positive endomembranes from 20 cells (**g**), Sec13-positive endomembranes from 53 cells (**h**) and Rab6-positive endomembranes from 82 cells (**i**). Scale bars, 10 μm.

Next, to compare density maps across experiments, we plotted the 50% density contour of CD63 for five independent experiments in two and three dimensions (**Fig. 1g**,**h**). Both 2D and 3D density maps of CD63 were highly reproducible, indicating well-defined organization of endomembranes.

Validation of the density estimation method

To validate the method's ability to reveal endomembranous architecture, we analyzed compact cellular structures whose organization is easily recognized. We applied density estimation to the Golgi apparatus and the centrosome using the markers GM130 (a Golgi matrix protein) and γ-tubulin, respectively. The centrosome is not an endomembranous structure, but as its coordinates can be determined in each cell, the average spatial distribution in two and three dimensions can be calculated using density estimation. Average 2D organization of the Golgi and the centrosome in crossbow-shaped RPE-1 cells has been previously reported[16]. In that work, the average intensity of each pixel had been calculated over stacks of multiple 2D images of independent cells using the same given marker proteins[16]. We used 69 cells to estimate the 2D density map of GM130-positive membranes and γ-tubulin, which revealed a Golgi and centrosome organization that was very similar to that previously described[16] (**Supplementary Fig. 2a**–**c**), validating our approach.

Our density approach enabled analysis of structures of different intensities, including non-homogenous populations, demonstrating its advantage in comparison to common intensity-based approaches. Moreover, with our approach, there was no loss of image sharpness that is a consequence of intensity averaging. Lastly, in comparison to previous work[16], our 3D analysis provided additional spatial information about the 3D organization of the Golgi and the centrosome in standardized micropatterned cells (**Supplementary Fig. 2d**–**f**). This opens the way to future studies on Golgi-centrosome organization in 3D cellular model systems.

Density maps reveal steady-state endomembrane organization

To establish the global subcellular endomembrane organization in crossbow-polarized cells, we applied density estimation to several marker proteins, which have been well-characterized as membrane-associated proteins of their respective endomembrane compartments. We considered Rab5, a small GTPase that specifically localizes to early endosomes[21], Sec13, which marks endoplasmic reticulum exit sites[22], and Rab6-positive structures. Rab6 is found on the *trans*-Golgi network as well as on transport carriers for either secretion or retrograde transport[23–25].

The 2D and 3D density estimates for each labeled compartment were highly reproducible (**Supplementary Fig. 3**) and differed from each other (**Fig. 2**). Rab5-associated signals were evenly distributed without preference for adhesive or nonadhesive regions (**Fig. 2d**,**g**). As the cell is thickest in the center, both the fluorescence projection and our 2D maps overestimate the concentration of Rab5-positive structures in the cell center; 3D estimation removed this bias, showing the inherent advantage of such an approach. In 2D and 3D density representations, Sec13 was highly concentrated around the nucleus (**Fig. 2e**,**h**), in agreement with the fact that the endoplasmic reticulum extends from the nuclear envelope and surrounds the Golgi. Density estimation of all Rab6-positive structures revealed central density corresponding to the Golgi and peripheral density owing to transport carriers (**Fig. 2f**,**i**). Whereas the Golgi density was similar to the GM130 map (**Supplementary Fig. 4m**–**o**), the density for Rab6-positive transport carriers was almost entirely found at adhesive areas of the crossbow pattern. In particular, transport carriers concentrated at the three corner points corresponding to main adhesion sites of actin stress fibers[16]. We also applied density mapping to HeLa and MDCK cells (**Supplementary Fig. 5**) and found that the organization of all marker proteins was similar to that in RPE-1 cells but cell type–specific features such as the shape of the

Figure 3 | Comparison of 'characteristic territories' and 'characteristic volumes' of endomembranes on crossbow-shaped patterns. (**a**,**b**) Characteristic territories of CD63-positive and Rab5-positive endosomes (**a**) and of Sec13-positive and Rab6-positive endomembranes (**b**). MVB, multivesicular bodies; EE, early endosomes; ERES, endoplasmic reticulum exit sites; TGN, *trans*-Golgi network; TC, transport carriers. Scale bars, 10 μm. (**c**) Standardized 2D cellular map. (**d**,**e**) 'Characteristic volume' of CD63-positive and Rab5-positive endosomes (**d**) and of Sec13-positive and Rab6-positive endomembranes (**e**). (**f**) Standardized 3D cell model. (**g**–**i**) Side views of maps shown in **d**–**f**, respectively. (**j**) Estimated MISE for 2D (left) and 3D (right) density estimation of all analyzed endomembranes as a function of the number of cells analyzed. Error bars, s.e.m.; *n* values are indicated in the figure.

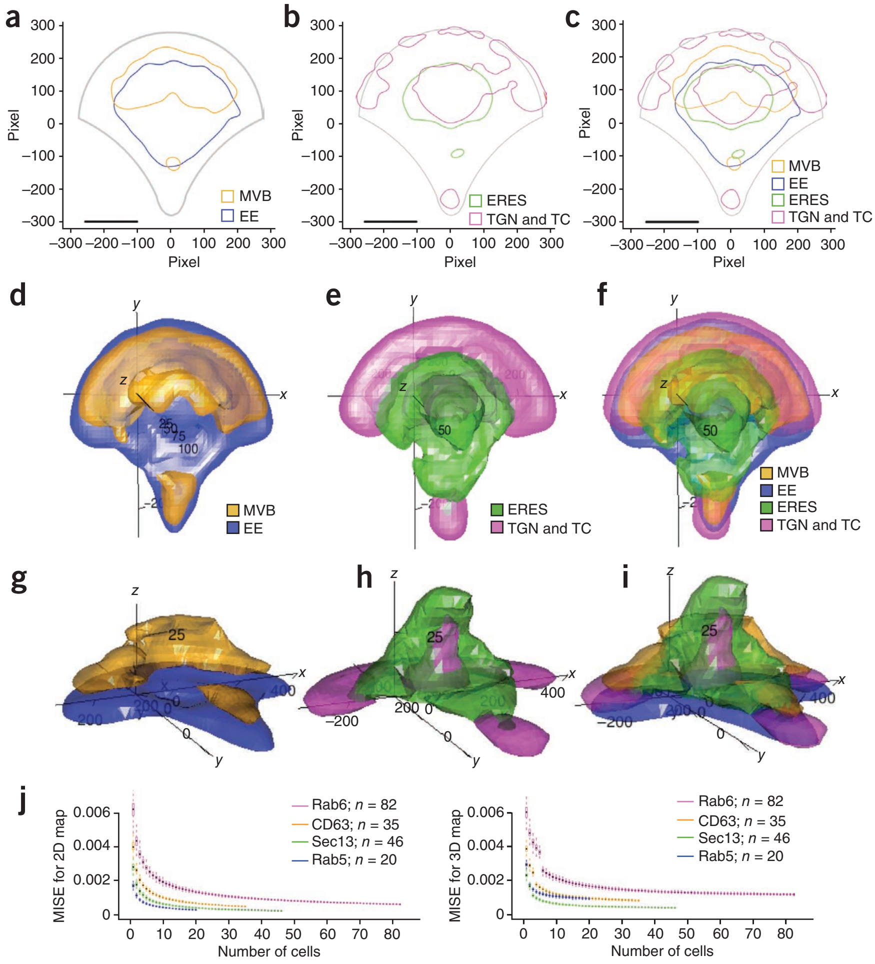

nucleus were apparent, which was the case for Sec13 (**Supplementary Fig. 5g–l**).

To visualize densities of all analyzed endomembranes in one standardized cell (**Fig. 3**), we defined the 'characteristic territory' and 'characteristic volume' representing the 50% contours of the 2D and 3D density estimates, respectively, and calculated them for each marker. We superposed CD63-positive multivesicular bodies with Rab5-positive early endosomes to compare different endosomal populations (**Fig. 3a**,**d**,**g**), and Sec13-marked endoplasmic reticulum exit sites with Rab6-positive Golgi membranes and transport carriers to visualize the spatial relationship between the endoplasmic reticulum, the Golgi apparatus and Golgi-derived transport carriers (**Fig. 3b**,**e**,**h**). We also combined all marker protein maps (**Fig. 3c**,**f**,**i**), which showed that different endomembranous subpopulations occupied specific regions of a standardized cell. The statistical error for all marker proteins reached asymptotic behavior before data for all cells were included (**Fig. 3j**), suggesting that in all cases the density estimation represented the underlying endomembranous organization with high fidelity. As density maps of all endomembrane populations did not drastically change upon addition of the data for the last analyzed cells and were reproducible in independent experiments, construction of a standardized cell model required only several tens of cells.

Endomembranous organization in circular cells

On crossbow-shaped patterns, organization of CD63 and Rab6-positive transport carriers depended strongly on the adhesion geometry (**Figs. 1** and **2c**,**f**,**i**). In particular, Rab6-positive transport carriers were not dense at nonadhering edges (**Fig. 2c**,**f**,**i**). We investigated how organization of these endomembranes was affected by changing the geometry of the pattern to a ring-shaped pattern with a continuous adhesive edge (**Supplementary Fig. 1b**). As this pattern is symmetric in all directions, we used the center of the pattern as the only alignment reference. CD63 as well as Rab6 (**Fig. 4a–j**) had a continuous round organization as a consequence of the imposed round attachment region of the pattern. As with the crossbow pattern, the CD63 steady-state distribution was interior to that of Rab6-positive transport carriers (**Fig. 4k**,**l** and **Supplementary Fig. 4a–c**). This indicates that CD63 and Rab6-positive endomembranous organization was partly adhesion-dependent but that the intrinsic relationship between endomembranes was to some extent conserved.

Remodeling of organization upon cytoskeletal disruption

To test the method's potential to detect changes in steady-state subcellular organization, we monitored Rab6-positive structures upon depolymerization of the cytoskeleton (**Fig. 5** and **Supplementary Videos 1–3**). Rab6-positive transport carriers move along microtubules from the Golgi to the cell periphery[17,24,25] where some of them interact with cortical proteins and subsequently fuse with the plasma membrane[24]. We treated cells with nocodazole (**Fig. 5f–j**) or cytochalasin D (**Fig. 5k–o**), which respectively disrupt microtubules or actin filaments. We applied the drugs at concentrations that did not alter cell shape. As expected, treatment with nocodazole fragmented the Golgi and redistributed Rab6-positive transport carriers from the cell periphery to the cell center (**Fig. 5f–j**). Actin disruption removed transport carriers from the most peripheral sites of cell adhesion, without strongly affecting global organization (**Fig. 5k–o**).

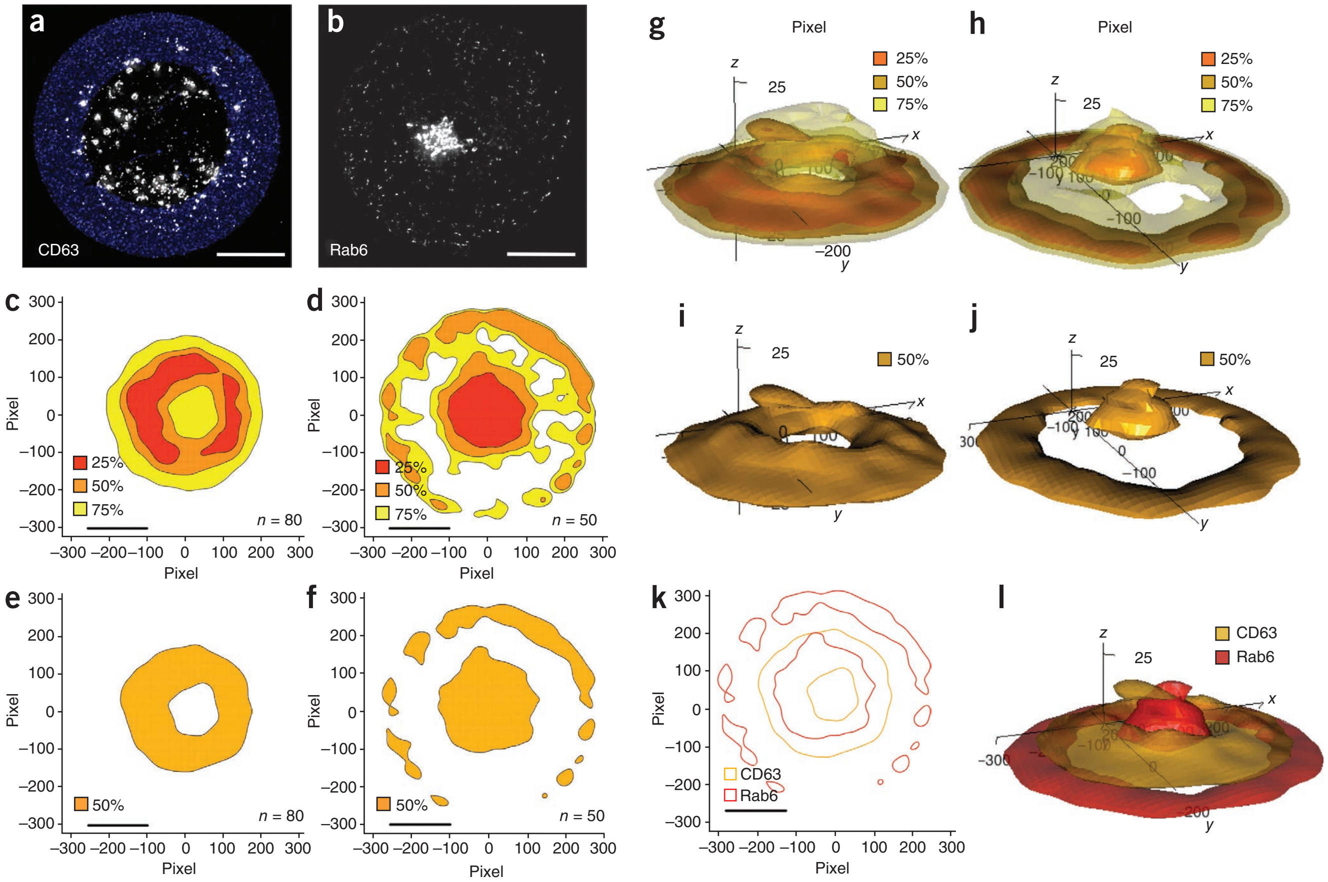

Figure 4 | Analysis of CD63- and Rab6-positive endomembranes in circular cells. (**a**,**b**) Maximum intensity projection of the deconvolved fluorescence of CD63 (white) and the fluorescently marked circular pattern (blue) (**a**) and Rab6-positive (**b**) endomembranes. (**c**,**d**) The 2D density estimations of CD63-positive endosomes from 80 cells (**c**) and Rab6-positive endomembranes from 50 cells (**d**). (**e**,**f**) 'Characteristic territory' of CD63-positive (**e**) and Rab6-positive endomembranes (**f**). (**g**,**h**) The 3D density estimations of CD63-positive (**g**) and Rab6-positive (**h**) endomembranes. (**i**,**j**) 'Characteristic volume' of CD63-positive (**i**) and Rab6-positive (**j**) endomembranes. (**k**,**l**) Standardized 2D cellular map (**k**) and 'characteristic volume' (**l**) of CD63-positive and Rab6-positive endomembranes. Scale bars, 10 μm.

This was consistent with classical analyses under which actin disruption was previously reported not to influence intracellular movement of Rab6-positive transport carriers[24].

We adapted and implemented a recently described statistical test[26] to quantitatively evaluate the significance of the observed difference. Essentially, the test compares a distance function between pairs of points from different experimental conditions with a distance function between pairs of points from the same experimental condition. We calculated the test statistic between untreated cells and either 50 cytochalasin D–treated cells with 13,755 structures or 47 nocodazole-treated cells with 10,941 structures. This gave a P value of 0 for both the cytochalasin D and nocodazole treatments, detecting differences between treated and untreated cells at all usual confidence levels (0.05, 0.01 and 0.001). Indeed, we obtained an average P value of less than 0.004 when analyzing data for only 20 cytochalasin D–treated cells or five nocodazole-treated cells (**Fig. 5p**). Control experiments using untreated cells in the place of the test set showed that the average P value remained around 0.5, as would be expected if the approximated null distribution was close to the true null distribution. Thus, changes in intracellular distribution of Rab6-positive transport carriers owing to microtubule and actin disruption were significant ($P = 0$ when analyzing all available cells), showing the power of our density-based standardized cell approach. In particular, unlike with previous classical analyses, we observed a statistically significant ($P = 0$) change in intracellular distribution of Rab6-positive transport carriers resulting from actin disruption.

We comprehensively benchmarked the statistical method on these two datasets, as well as the dataset for CD63-positive endosomes (**Supplementary Fig. 6**). We measured the performance of the statistical test when varying both the number of treated cells used and variance parameter σ^2. For 100 random trials, for all of $\sigma^2 = 50$, 200 and 800, we obtained an average $P < 0.004$ for all three datasets with only 20 treated cells (**Supplementary Fig. 6**). Thus, significant morphological alterations could be consistently detected with as few as 20 cells.

To determine the advantage of cellular standardization by micropatterning, we performed the same statistical test on nonpatterned cells (**Fig. 5q**). For strong phenotypes, such as Golgi dispersion after nocodazole treatment, we could detect significant ($P < 0.001$) differences, although data for eight times more cells were needed. In contrast, subtle differences, such as those seen upon treatment with cytochalasin D, were not detectable in unconstrained cells. Therefore, micropatterning in combination with computational analysis is a powerful tool to detect subtle changes in steady-state endomembranous organization.

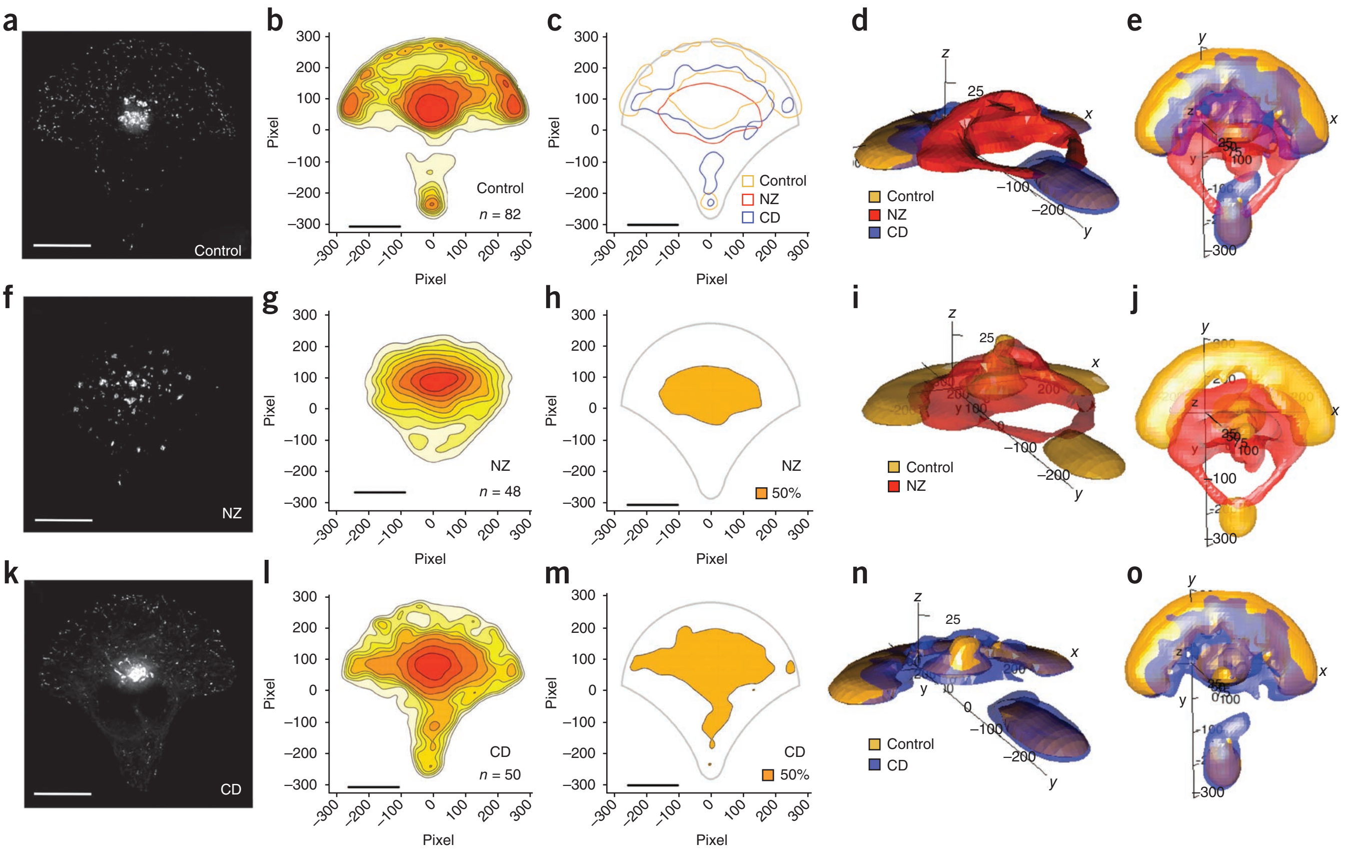

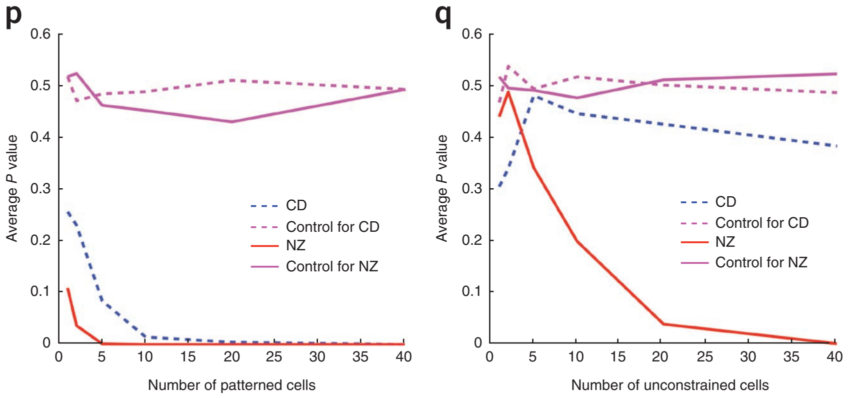

Figure 5 | Changes of Rab6-positive endomembranes upon cytoskeletal disruption. (**a**–**o**) Maximum intensity projection of the deconvolved fluorescence of Rab6-positive endomembranes without treatment (control) (**a**), upon nocodazole treatment (NZ; **f**) and cytochalasin D treatment (CD; **k**). For each of these datasets, we plotted a 2D density estimation (**b**,**g**,**l**). The probability contours represent the smallest regions in which 10% (red) to 90% (yellow) of endomembranes are found. Then, we plotted the 50% characteristic territory (**c**,**h**,**m**) and 50% characteristic volume (**d**,**i**,**n**) for these data alone or in combinations for comparison, as indicated. Top views of the characteristic volumes in **d**, **i** and **n** are shown in **e**, **j** and **o**, respectively. The data for cells without treatment is the same as that plotted in **Figure 2f**. Scale bars, 10 µm. (**p**,**q**) Test statistic of micropatterned (**p**) and unconstrained (**q**) cells as a function of the number of cells analyzed. *P* values for NZ and CD treatments as well as untreated control cells are given for $\sigma^2 = 50$.

DISCUSSION

Many studies have found alterations in the cellular architecture during physiological and pathological processes[27]. But the complex topology of endomembranes hinders precise quantification of their organization and alterations in pathological situations such as cancer.

Our results with micromanipulation-normalized cells favor the hypothesis that cellular trafficking components are highly organized and become visibly polarized once cells are immobilized and forced to take a reproducible shape by an imposed geometry. This is consistent with previous studies in the model system of polarized MDCK cells, which revealed several spatially distinct biosynthetic and recycling compartments[28], and with the fact that intracellular compartments show a high degree of organization in a variety of tissues of living organisms[1]. Our approach revealed that endomembrane organization is dependent on the adhesion geometry of the extracellular matrix that is known to be important in the establishment of cell polarity, instrumental for normal cell function and tissue homeostasis. Unlike studies in MDCK cells, which do not allow changes in the adhesion geometry, our setup allows the investigation of mechanisms that position endomembranes in response to polarity clues.

Our approach provides a powerful way to visualize endomembraneous alterations. The density estimation obtained for cells with disrupted actin showed retraction of transport carriers from peripheral adhesive areas, indicating that Rab6A-positive secretory vesicles were entrapped at the edge of the cell by actin filaments. This is consistent with actin filaments being known to be ordered close to the cell surface and to spread out transport carriers[29]. Previously, alterations in intracellular trafficking have been revealed indirectly by missorting of marker proteins. The direct and intuitive visualization of alterations in endomembrane distribution provided by our method is therefore extremely useful in the assignment of functional roles to trafficking components. It will be interesting to investigate whether patterned cells could be used as references to rapidly highlight pathological disorders during malignant development. As estimations can be performed in three dimensions, our methodology is also applicable to other cell lines and apical-basal polarity model systems that show reproducible 3D organization.

Endomembrane organization is strictly defined and can be used to detect subtle cellular perturbations that are statistically significant. This paves the way to high-throughput analyses of phenotypic alteration upon chemical compound or short interfering RNA treatments. This analysis is well-suited for large populations. As it is the total number of structures that is important for the reliability of density maps and the power of the statistical test, the number of cells required for analysis depends on the number of structures per cell.

State-of-the-art high-content and high-throughput approaches are often hindered by statistical concerns, as it is difficult to determine the exact number of cells that have to be measured per sample. Our approach shows that, for populations with large numbers of structures, only 20 cells were required to define stable organization and to uncover significant ($P < 0.004$) differences in endomembrane density induced by drug treatment. Therefore, the density framework in micropatterned cells has the potential to become a gold-standard in the quantitative analysis of high-throughput data. Attempts are underway to incorporate this method into a screening workflow for identification of factors that sustain the steady-state organization of endomembranes.

METHODS

Methods and any associated references are available in the online version of the paper at http://www.nature.com/naturemethods/.

Note: Supplementary information is available on the Nature Methods website.

ACKNOWLEDGMENTS

We acknowledge L. Sengmanivong of the Nikon Imaging Centre at Institut Curie–Centre National de la Recherche Scientifique and V. Fraisier of the Plate-forme Imagerie Cellulaire et Tissulaire–Infrastructures en Biologie Santé et Agronomie Imaging Facility for their extensive help with microscopes and in particular their help using the deconvolution service of the facility. We thank J.-B. Sibarita for advice on image analysis including use of the multidimensional image analysis program and fruitful discussion during early phases of the project; I. Brito for statistical advice; W. Hong (Institute of Molecular and Cell Biology, Singapore) for providing the Sec13 antibody; M. Piel, A. Azioune and J. Fink for help with microprinting; and G. Egea, S. Miserey, A. Echard and J. Enninga for critical reading of the manuscript. K.S. received funding from the Fondation pour la Recherche Médicale en France and Association pour la Recherche sur le Cancer. This project was supported by grants from the Centre National de la Recherche Scientifique and Institut Curie.

AUTHOR CONTRIBUTIONS

K.S. and B.G. designed the research, K.S. performed the experiments and analysis and wrote the manuscript, T.D. developed the density calculation, K.B. developed the statistical analysis and edited the manuscript, S.B. adjusted patterning techniques and M.B. contributed to the conception of the work.

COMPETING FINANCIAL INTERESTS

The authors declare no competing financial interests.

1. Bornens, M. Organelle positioning and cell polarity. *Nat. Rev. Mol. Cell Biol.* **9**, 874–886 (2008).
2. Caviston, J.P. & Holzbaur, E.L. Microtubule motors at the intersection of trafficking and transport. *Trends Cell Biol.* **16**, 530–537 (2006).
3. Lanzetti, L. Actin in membrane trafficking. *Curr. Opin. Cell Biol.* **19**, 453–458 (2007).
4. Ross, J.L., Ali, M.Y. & Warshaw, D.M. Cargo transport: molecular motors navigate a complex cytoskeleton. *Curr. Opin. Cell Biol.* **20**, 41–47 (2008).
5. Insall, R.H. & Machesky, L.M. Actin dynamics at the leading edge: from simple machinery to complex networks. *Dev. Cell* **17**, 310–322 (2009).
6. Schmoranzer, J. *et al.* Par3 and dynein associate to regulate local microtubule dynamics and centrosome orientation during migration. *Curr. Biol.* **19**, 1065–1074 (2009).
7. Egea, G., Lazaro-Dieguez, F. & Vilella, M. Actin dynamics at the Golgi complex in mammalian cells. *Curr. Opin. Cell Biol.* **18**, 168–178 (2006).
8. Rivero, S., Cardenas, J., Bornens, M. & Rios, R.M. Microtubule nucleation at the cis-side of the Golgi apparatus requires AKAP450 and GM130. *EMBO J.* **28**, 1016–1028 (2009).
9. Semenova, I. *et al.* Actin dynamics is essential for myosin-based transport of membrane organelles. *Curr. Biol.* **18**, 1581–1586 (2008).
10. Taunton, J. Actin filament nucleation by endosomes, lysosomes and secretory vesicles. *Curr. Opin. Cell Biol.* **13**, 85–91 (2001).
11. Sachs, K., Perez, O., Pe'er, D., Lauffenburger, D.A. & Nolan, G.P. Causal protein-signaling networks derived from multiparameter single-cell data. *Science* **308**, 523–529 (2005).
12. Sigal, A. *et al.* Variability and memory of protein levels in human cells. *Nature* **444**, 643–646 (2006).
13. Snijder, B. *et al.* Population context determines cell-to-cell variability in endocytosis and virus infection. *Nature* **461**, 520–523 (2009).
14. Liu, W.F. & Chen, C.S. Cellular and multicellular form and function. *Adv. Drug Deliv. Rev.* **59**, 1319–1328 (2007).
15. Thery, M., Pepin, A., Dressaire, E., Chen, Y. & Bornens, M. Cell distribution of stress fibres in response to the geometry of the adhesive environment. *Cell Motil. Cytoskeleton* **63**, 341–355 (2006).
16. Thery, M. *et al.* Anisotropy of cell adhesive microenvironment governs cell internal organization and orientation of polarity. *Proc. Natl. Acad. Sci. USA* **103**, 19771–19776 (2006).
17. Racine, V. *et al.* Visualization and quantification of vesicle trafficking on a three-dimensional cytoskeleton network in living cells. *J. Microsc.* **225**, 214–228 (2007).
18. Bowman, A.W. & Foster, P. Density based exploration of bivariate data. *Stat. Comput.* **3**, 171–177 (1993).
19. Hyndman, R. Computing and graphing highest density regions. *Am. Stat.* **50**, 120–126 (1996).
20. Pols, M.S. & Klumperman, J. Trafficking and function of the tetraspanin CD63. *Exp. Cell Res.* **315**, 1584–1592 (2009).
21. Chavrier, P., Parton, R.G., Hauri, H.P., Simons, K. & Zerial, M. Localization of low molecular weight GTP binding proteins to exocytic and endocytic compartments. *Cell* **62**, 317–329 (1990).
22. Tang, B.L. *et al.* The mammalian homolog of yeast Sec13p is enriched in the intermediate compartment and is essential for protein transport from the endoplasmic reticulum to the Golgi apparatus. *Mol. Cell. Biol.* **17**, 256–266 (1997).
23. Antony, C. *et al.* The small GTP-binding protein rab6p is distributed from medial Golgi to the *trans*-Golgi network as determined by a confocal microscopic approach. *J. Cell Sci.* **103**, 785–796 (1992).
24. Grigoriev, I. *et al.* Rab6 regulates transport and targeting of exocytotic carriers. *Dev. Cell* **13**, 305–314 (2007).
25. White, J. *et al.* Rab6 coordinates a novel Golgi to ER retrograde transport pathway in live cells. *J. Cell Biol.* **147**, 743–760 (1999).
26. Gretton, A., Borgwardt, K.M., Rasch, M.J., Schoelkopf, B. & Smola, A. A kernel method for the two-sample problem. *Advances in Neural Information Processing Systems 19: Proceedings of the 2006 Conference* 513–520 (MIT Press, Cambridge, Masssachusetts, USA, 2007).
27. Wodarz, A. & Näthke, I. Cell polarity in development and cancer. *Nat. Cell Biol.* **9**, 1016–1024 (2007).
28. Rodriguez Boulan, E. & Sabatini, D.D. Asymmetric budding of viruses in epithelial monlayers: a model system for study of epithelial polarity. *Proc. Natl. Acad. Sci. USA* **75**, 5071–5075 (1978).
29. Snider, J. *et al.* Intracellular actin-based transport: how far you go depends on how often you switch. *Proc. Natl. Acad. Sci. USA* **101**, 13204–13209 (2004).

ONLINE METHODS

Cells and reagents. Retinal pigment epithelial (RPE-1) cells (Invitrogen) were grown in DMEM/F12 medium supplemented with 10% FBS and 1% ampicillin-streptomycin. A EGFP-Rab6A–expressing stable cell line was generated by transfection of the plasmid pEGFP-Rab6Awt[25] into RPE-1 or HeLa cells and selection with 500 μg ml^{-1} geneticin. Pattern production and cell plating conditions were as previously described[30]. To depolymerize microtubules, nocodazole (NZ) was added to a final concentration of 20 μM and cells were left at 4 °C for 60 min. Cells were then transferred to 37 °C and incubated for 1 h. To disrupt the actin cytoskeleton, cytochalasin D (CD) was added to a final concentration of 0.5 μM and cells were incubated at 37 °C for 1 h. Cells were fixed with 4% (wt/vol) paraformaldehyde (PFA) for 15 min before either being processed for immunofluorescence staining (CD63, Rab5, Sec13, GM130 and γ-tubulin) or immediate image analysis (Rab6).

Immunofluorescence staining. PFA-fixed cells were quenched with 0.05 M NH_4Cl, washed three times with PBS (pH 7.4) and permeabilized in PBS with 2% BSA and 0.05% saponin, before incubation with primary and Alexa Fluor 488–, Cy-3– or Cy-5–coupled secondary antibodies (Jackson ImmunoResearch). The primary antibodies used were anti-CD63 (Invitrogen), anti-GM130 (BD Biosciences), anti–γ-tubulin, anti-Rab5 (BD Biosciences) and anti-Sec13 (ref. 22). After three washes with PBS, coverslips were mounted on object holders with Moviol containing 0.0002 mg ml^{-1} DAPI.

Immunofluorescence image acquisition and analysis. Images were acquired with a wide-field Eclipse 90i Upright Microscope (Nikon) equipped for image deconvolution. Acquisition was performed using a 100× Plan Apo VC 1.4 oil objective and a highly sensitive cooled interlined charge-coupled device (CCD) camera (Roper CoolSnap HQ2). *Z*-dimension positioning was accomplished by a piezoelectric motor (LVDT, Physik Instrument) and a *z*-dimension series of images was taken every 0.2 μm. After deconvolution[31], images were segmented with the multidimensional image analysis (MIA) interface running under MetaMorph (Universal Imaging Corporation) based on wavelet decomposition[17]. Briefly, fluorescent objects were detected as fluctuations that are 15-fold larger than noise. The watershed function was routinely applied for CD63, Rab6 and GM130 to precisely detect individual structures in dense regions (and segment the Golgi apparatus in several structures).

Alignment of coordinates of endomembranes. Coordinates of the center of patterns were automatically extracted from 3D image stacks of micropatterns visualized with fluorescently labeled fibrinogen using a computational tool developed under ImageJ (W.S. Rasband, US National Institutes of Health). Briefly, first the most in-focus image of the 3D stack of fluorescently labeled patterns was chosen. Then, the image was automatically binarized after several steps of image processing. The ImageJ plugin Hough-Circles was used for center detection. In the case of the crossbow pattern, the angle of rotation was manually determined in each experiment.

Kernel density estimator. The probability density function *f* for each data sample (for example, CD63) of *n* coordinates X_1, X_2, …, X_n was estimated. We used a nonparametric, unbinned kernel density estimator[32]. The estimation was performed using the ks library (Duong, T; ks: kernel smoothing, R package version 1.6.3.) in R (R Development Core Team; R: a language and environment for statistical computing). At each of the data points, a kernel function *K* was centered. The kernel functions were then summed to form the kernel density estimator

$$\hat{f}_{\mathbf{H}}(x) = \frac{1}{n}\sum_{i=1}^{n} K_{\mathbf{H}}(x - X_i),$$

in which K_{H} is the Gaussian kernel with mean zero and variance matrix H**.** To estimate H (also known as the bandwidth), we used the plug-in selector in the ks library that has been shown to be reliable for 2D and 3D spatial distributions[33]. For visualizing kernel density estimates, we used probability contours[18,19]. Graphical representation in three dimensions was achieved using the rgl (D. Adler and D. Murdoch; rgl: 3D visualization device system (OpenGL), R package version 0.84) and misc3d (D. Feng and L. Tierney; misc3d: miscellaneous 3D plots, R package version 0.6–1) libraries (**Supplementary Note 1**).

Statistical error of kernel density estimation. The statistical error for kernel density estimates was determined by calculating the estimated mean integrated squared error (MISE) as a function of the number of cells analyzed. For the combined sample of the *n* endomembrane coordinates from *m* cells, we computed the average number of endomembranes per cell (*n*/*m*). This ratio was rounded to the nearest 100 cells for numerical convenience (CD63, 300; Rab5, 800; Sec13, 400; and Rab6, 200). To compute the estimated MISE for *j* cells, *j* = 1, 2, …, *m* we resampled *j* × (*n*/*m*) endomembrane coordinates from the total of *n* coordinates. This resampling was performed 100 times for each *j* to ensure statistical robustness.

Statistical analysis. As in the kernel density estimation, we supposed each data sample was a set of coordinates U_1, U_2, …, U_n (untreated) or T_1, T_2, …, T_n (treated) generated from underlying density functions f_U and f_T. The statistical test we propose[26] tests the null hypothesis: $f_U = f_T$. The test statistic MMD^2 (maximum mean discrepancy squared) is given by

$$\mathrm{MMD}^2 = \frac{1}{n(n-1)}\sum_{i \neq j}^{n}\left(k(U_i,U_j) + k(T_i,T_j) - k(U_i,T_j) - k(U_j,T_i)\right),$$

with *k* a Gaussian kernel:

$$k(A,B) = \exp\left(-\frac{\|A-B\|^2}{2\sigma^2}\right).$$

Intuitively, MMD^2 will be large if on average the first two terms of the summands are larger than the second two. This corresponds to untreated coordinates being closer on average to untreated than treated ones and vice versa. The larger the value of MMD^2, the more likely we are to reject the null hypothesis. This is quantified by estimating the null distribution in the following way: first, obtain supplementary untreated data U'_1, U'_2, …, U'_m, with *m* larger than 2*n*, then randomly select two disjoint sets of size *n* and calculate the value of MMD^2. Repeating this randomized step a sufficient number of times gives an approximation of the null distribution; we performed this step 100,000 times. An empirical *P* value could then be calculated. The value of σ^2 was fixed as $\sigma^2 = 50$, corresponding to $k(A, B) = 1$ when *A* and *B* coincide and $k(A, B) = \exp(-1)$ when *A* and *B* are exactly 10 pixel units apart. This choice of σ^2 corresponds biologically to deciding that the similarity (via MMD^2) of two sets of data points extracted from cells is predominantly determined by the pairs of points that are less than 10 pixel units apart. Outside this range, the maximum value of k (A, B) is 0.37, and decreases exponentially for pairs of points that are further and further apart. A more detailed explanation of the statistical methodology and comprehensive benchmarking of the method (including the influence of σ^2) on three datasets is available in **Supplementary Note 2**.

30. Azioune, A., Storch, M., Bornens, M., Théry, M. & Piel, M. Simple and rapid process for single cell micro-patterning. *Lab Chip* **9**, 1640–1642 (2009).
31. Sibarita, J.B. Deconvolution microscopy. *Adv. Biochem. Eng. Biotechnol.* **95**, 201–243 (2005).
32. Simonoff, J.S. *Smoothing Methods for Statistics*. (Springer, New York, 1996).
33. Duong, T. & Hazelton, M.L. Plug-in bandwidth matrices for bivariate kernel density estimations. *J. Nonparametr. Stat.* **17**, 17–30 (2003).

doi:10.1038/nmeth.1462